LETTER

Elucidating Reversible Electrochemical Redox of Li$_6$PS$_5$Cl Solid Electrolyte

Darren H. S. Tan,[†] Erik A. Wu,[†] Han Nguyen,[†] Zheng Chen,[†,‡] Maxwell A. T. Marple,[§] Jean-Marie Doux,[†] Xuefeng Wang,[†] Hedi Yang,[†] Abhik Banerjee,[*,†] and Ying Shirley Meng[*,†,‡]

[†]Department of NanoEngineering, University of California San Diego, La Jolla, California 92093, United States
[‡]Sustainable Power & Energy Center (SPEC), University of California San Diego, La Jolla, California 92093, United States
[§]Physical and Life Science Directorate, Lawrence Livermore National Laboratory, Livermore, California 94550, United States

Ⓢ *Supporting Information*

ABSTRACT: Sulfide-based solid electrolytes are promising candidates for all solid-state batteries (ASSBs) due to their high ionic conductivity and ease of processability. However, their narrow electrochemical stability window causes undesirable electrolyte decomposition. Existing literature on Li-ion ASSBs report an irreversible nature of such decompositions, while Li−S ASSBs show evidence of some reversibility. Here, we explain these observations by investigating the redox mechanism of argyrodite Li$_6$PS$_5$Cl at various chemical potentials. We found that Li−In | Li$_6$PS$_5$Cl | Li$_6$PS$_5$Cl−C half-cells can be cycled reversibly, delivering capacities of 965 mAh g^{-1} for the electrolyte itself. During charging, Li$_6$PS$_5$Cl forms oxidized products of sulfur (S) and phosphorus pentasulfide (P$_2$S$_5$), while during discharge, these products are first reduced to a Li$_3$PS$_4$ intermediate before forming lithium sulfide (Li$_2$S) and lithium phosphide (Li$_3$P). Finally, we quantified the relative contributions of the products toward cell impedance and proposed a strategy to reduce electrolyte decomposition and increase cell Coulombic efficiency.
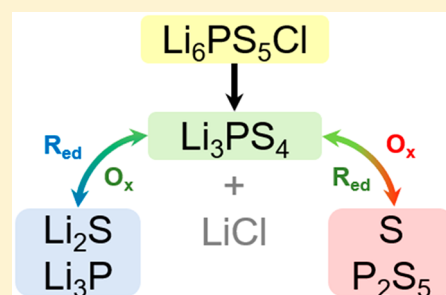
All solid-state batteries (ASSBs) show great promise to become the next-generation energy storage technology. Compared to conventional liquid electrolyte-based batteries, ASSBs utilizes nonflammable solid-state electrolytes (SSEs), which translate to improved safety and the ability to operate over a wider temperature range.[1,2] As such, recent years have seen much research focused on developing highly conductive SSEs as well as fundamental studies on their intrinsic electrochemical properties. Among these electrolytes, argyrodite Li$_6$PS$_5$Cl has attracted much attention due to its high ionic conductivity (>1 mS cm^{-1} at 298 K), ease of material synthesis, and low-temperature processability, which are critical requirements for scalable fabrication of ASSBs.[3−6] It is also a relatively well studied electrolyte material with detailed experimental literature on its synthesis parameters, crystalline structure, and mechanical properties.[3−6] However, its electrochemical interface and respective decomposition products against electrodes are not as well investigated. Although existing literature on the sulfide electrolyte−electrode interface focuses on the chemical reactions against lithium metal anodes or layered oxide cathodes,[5,7−10] knowledge of its intrinsic interfacial electrochemical properties crucial for designing sulfide-based ASSBs remains lacking.

Like most sulfide-based SSEs, Li$_6$PS$_5$Cl has a relatively narrow electrochemical stability window, causing it to decompose during cell cycling to form unwanted interfacial

oxidation or reduction products.[11−13] While these oxidation and reduction products have not been fully identified experimentally due to its amorphous and buried nature, they have been predicted by computational density functional theory (DFT) studies done on common SSEs (e.g., Li$_{10}$GeP$_2$S$_{12}$, Li$_7$P$_3$S$_{11}$, Li$_3$PS$_4$, Li$_6$PS$_5$Cl).[13,14] Despite its ability to form passivating interfaces enabling their use in ASSBs without forming electronic pathways that short the cell, their interfacial properties are still unfavorable for cell performance due to large impedance growth and poor first cycle coulombic efficiencies.[9,15] Current reports on sulfide-based Li-ion ASSBs show an irreversible SSE decomposition forming on the interface during the first charge.[9,16] However, recent studies have suggested the reversible nature of this decomposition, giving rise to high specific cell capacities.[5,6,17−19] This electrolyte decomposition-derived capacity is commonly seen in solid-state Li−S battery reports using sulfide-based SSEs, where capacities higher than the cathode's theoretical capacities of Li$_2$S and S were previously reported (Figure 1a). The extra reversible capacity likely arises as result of contributions from reversible electrolyte decomposition beyond the first cycle as both Li−S and sulfide-based SSE
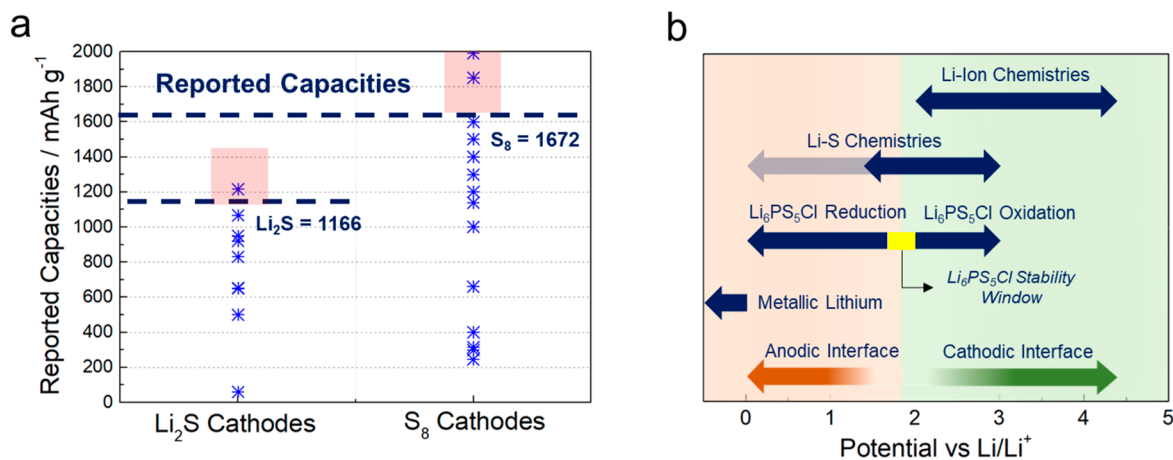
Figure 1. (a) Reported first cycle discharge capacities of representative solid-state Li−S batteries in the literature.[6,18,20−44] Dotted lines represent the theoretical capacity of Li$_2$S and S. (b) Illustration of electrochemical operating windows for Li$_6$PS$_5$Cl, Li−S, and Li-ion chemistries.
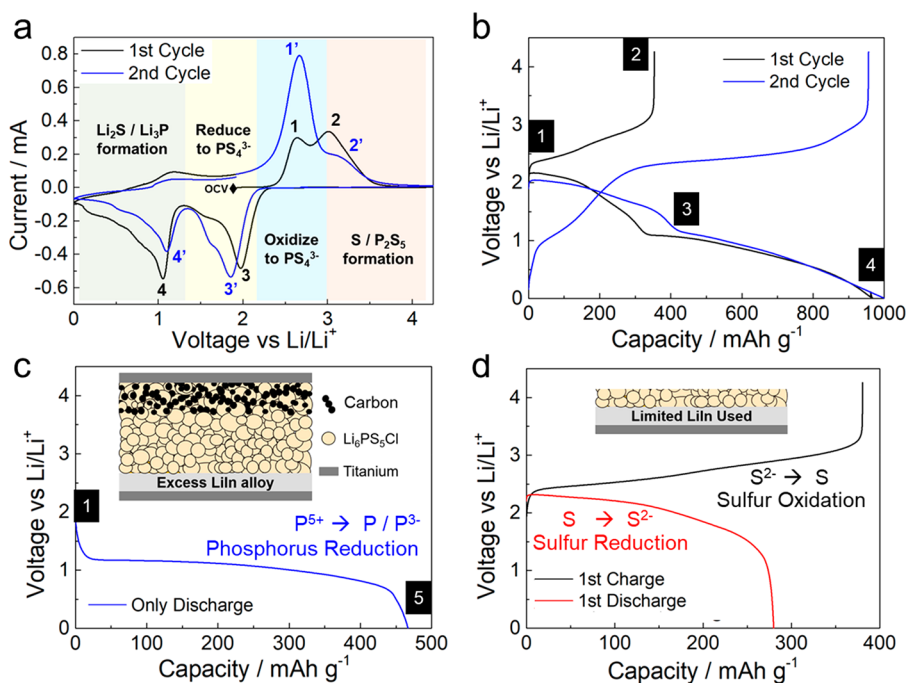

Figure 2. (a) Cyclic voltammograms for the first two cycles; the voltage was swept between 0 and 4.2 V (vs Li/Li$^+$) at 100 μV s^{-1} starting from the OCV. (b) First and second voltage profiles of the Li−In | Li$_6$PS$_5$Cl | Li$_6$PS$_5$Cl−C half-cell. Cycling was done between 0 and 4.2 V (vs Li/Li$^+$) at room temperature and a current density of 0.25 mA cm^{-2}. (c) First direct discharge curve showing one voltage plateau at 1.0 V for excess Li$^+$ source, indicating phosphorus species reduction. (d) First charge and discharge curves showing one voltage plateau at 2.0 V for a limited Li$^+$ source, indicating sulfur species redox. Marked numbers 1−5 represent potentials where Li$_6$PS$_5$Cl was extracted for characterization.

redox (S/S^{2-}) occur simultaneously during cycling over the same voltage range. A summary of capacities for Li−S ASSBs in the literature is illustrated in Table S1.

The reversible/irreversible observations made in these reports can be rationalized by comparing the operating voltage ranges of batteries used (Figure 1b). Comparing typical voltage ranges used in Li-ion and Li−S batteries against redox potentials of sulfide electrolytes such as Li$_6$PS$_5$Cl, it becomes clear that oxidative decomposition seen in Li-ion ASSBs would be perceived as irreversible. Likewise, oxidative and reductive decomposition of SSEs in ASSBs with lower operating voltages such as Li−S batteries would be reversible and detected by extra capacities reported from the S or Li$_2$S cathodes,

respectively. However, because both SSE decomposition and Li−S redox occur at overlapping voltage windows, it is hard to characterize and deconvolute the capacity contributions from each component. Furthermore, there is poor understanding of the redox mechanism of Li$_6$PS$_5$Cl electrolyte alone, with studies mainly investigating its first cycle oxidation against layered oxide electrodes or its chemical reactions against metallic lithium. Thus, it is vital to investigate the intrinsic electrochemical decomposition of Li$_6$PS$_5$Cl itself and its reversibility at typical cathode and anode potentials, without any contributions from the active electrodes.

Here, we use various characterization tools to experimentally observe the decomposition redox of Li$_6$PS$_5$Cl and propose a
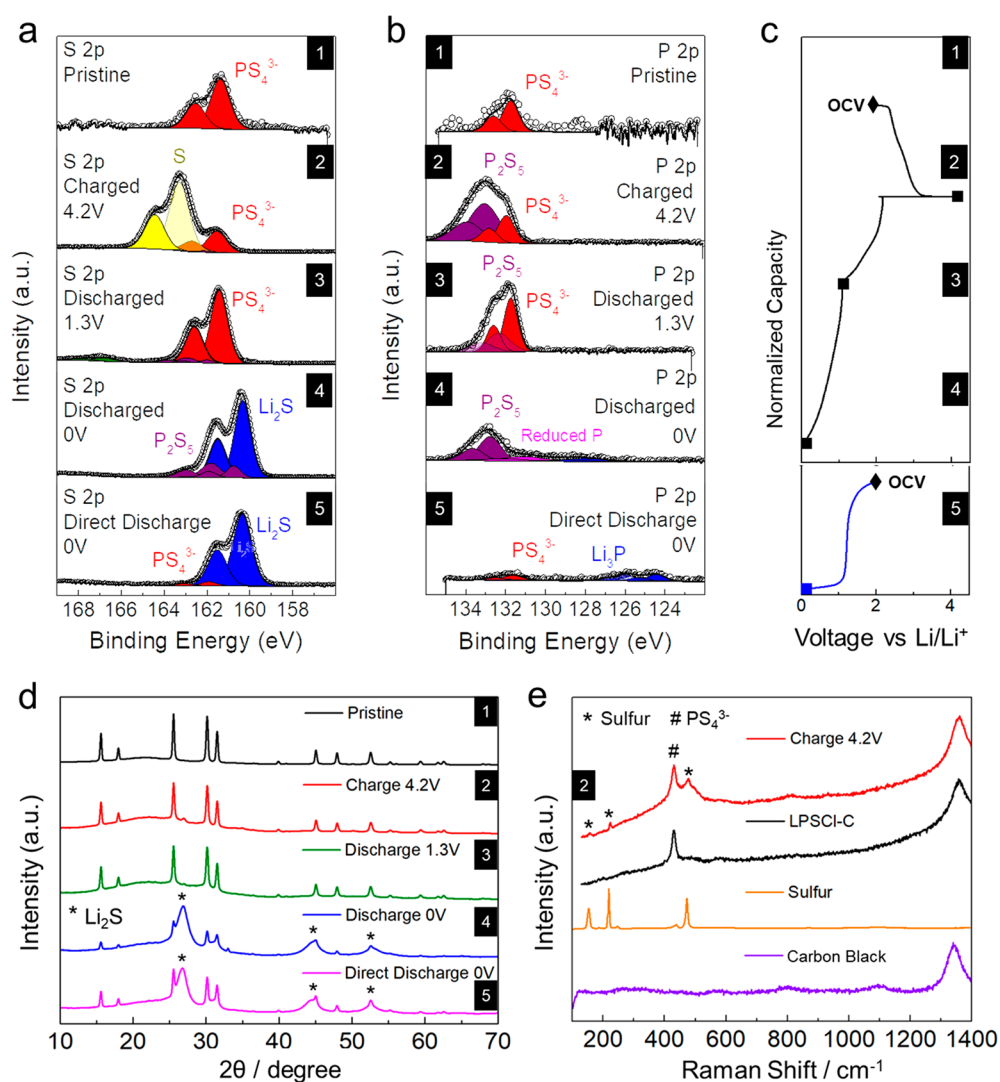
Figure 3. XPS spectra showing the binding energies of Li_6PS_5Cl at different cycling potentials. (a) Sulfur 2p region. (b) Phosphorus 2p region. (c) Cycling voltage profile for reference. (d) XRD patterns at different cycling potentials. Li_2S can be identified as a reduced product. (e) Raman spectra at a fully charged state. Sulfur is identified as an oxidized product. Raman spectra from the pristine cathode, sulfur, and CB are displayed for reference.

reaction pathway that helps shed light on its capacity contribution. The decomposition products at various potentials are identified, and cell level properties are evaluated by isolating species at the anode and cathode interface to quantify their relative contributions to cell impedance. Finally, we demonstrate a method to reduce electrolyte decomposition in ASSBs and demonstrate its effectiveness in a typical Li−In | Li_6PS_5Cl | NCM811 cell. This study is fundamentally important to analyze thermodynamically driven interface product formation at electrodes of ASSBs and inform strategies for interfacial engineering and cell design.

Electrochemical Redox of Li_6PS_5Cl. To investigate the reversible decomposition redox of Li_6PS_5Cl, a half-cell setup was used with Li−In as the anode and carbon black (CB) (30 wt %) mixed with Li_6PS_5Cl (70 wt %) on the cathode. Cyclic voltammetry (CV) was performed on the Li−In | Li_6PS_5Cl | Li_6PS_5Cl−C cell (Figure 2a). Starting at the open-circuit voltage (OCV), a positive sweep yielded two oxidative peaks (1, 2) at 2.6 and 3.0 V, while the negative sweep showed two reductive peaks (3, 4) at 2.0 and 1.1 V, respectively. During the second cycle, the first oxidative peak (1′) appeared more

intense, which is associated with a higher charging capacity, followed by a smaller oxidative peak (2′). There is a slight shift of the first reductive peak (3′) to lower voltage, indicating changes in cell polarization after oxidation. These observations were also validated with galvanostatic cell cycling (Figure 2b), where increased charge capacity and lowered discharge voltage at the second cycle were found.
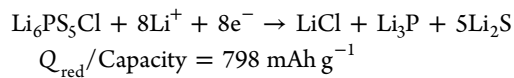
From Figure 2b, the first galvanostatic charge/discharge cycles of the Li_6PS_5Cl−C electrode yielded large capacities of 354 and 968 mAh g^{-1}, respectively, while the second cycle yielded 956 and 1002 mAh g^{-1}, respectively. The first charge voltage plateau starts at an oxidation potential of 2 V, which agrees with DFT calculations in the literature.[13] This oxidation potential has also been reported in work studying sulfide decomposition in Li-ion ASSBs.[15] Interestingly, a typical discharge cycle (Figure 2b) displays two plateaus, one between 2.2 and 1.3 V and a second between 1.3 and 0 V, corresponding to the two reductive peaks in Figure 2a. This indicates two distinct thermodynamic reduction reactions at each respective voltage. Such a double discharge plateau has not been observed in previous literature on either sulfide SSE
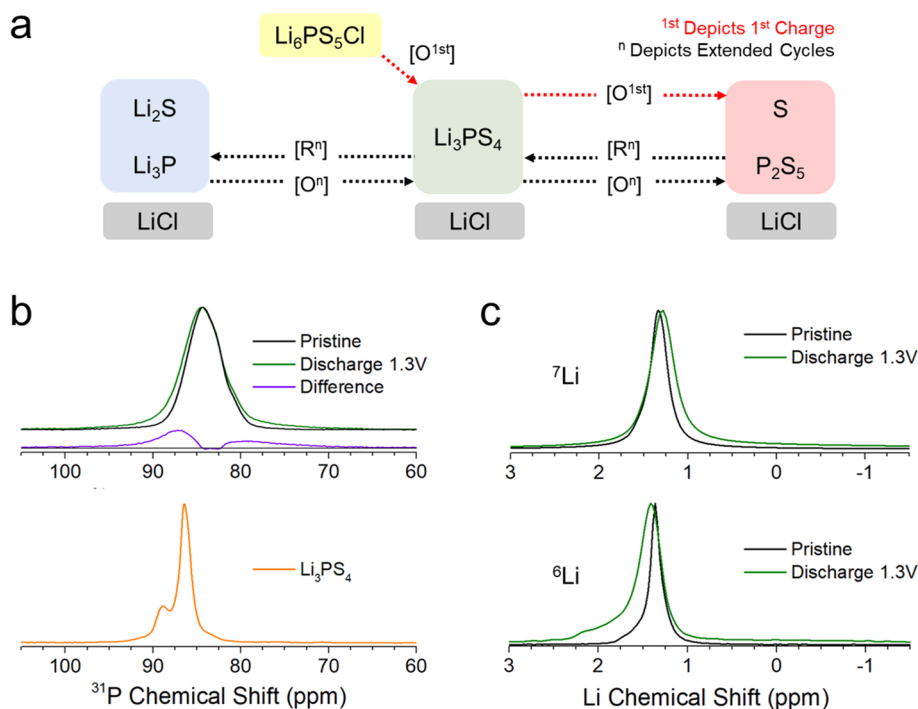
Figure 4. (a) Redox reaction pathway of Li_6PS_5Cl for the first charge and subsequent cycles. (b) (Top) ^{31}P MAS NMR spectra of pristine and mid-discharged Li_6PS_5Cl. (Bottom) ^{31}P MAS NMR spectrum of reference Li_3PS_4 containing both γ and β phases. (c) (Top) ^{7}Li MAS NMR spectra of pristine and mid-discharged Li_6PS_5Cl. (Bottom) ^{6}Li MAS NMR spectrum revealing the rise of a broad peak centered at 0.81 ppm. Expanded chemical shift ranges can be found in the SI.

redox studies[11,19,45] or Li−S batteries work using sulfide SSEs[6,33] for reasons that will be discussed later.

Theoretical Capacity of Li_6PS_5Cl Oxidation/Reduction

$$Li_6PS_5Cl \rightarrow LiCl + \frac{1}{2}P_2S_5 + \frac{5}{2}S + 5Li^+ + 5e^-$$
$$Q_{ox}/Capacity = 499 \text{ mAh g}^{-1}$$

$$Li_6PS_5Cl + 8Li^+ + 8e^- \rightarrow LiCl + Li_3P + 5Li_2S$$
$$Q_{red}/Capacity = 798 \text{ mAh g}^{-1}$$
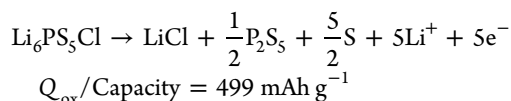
To understand this phenomenon, we hypothesize that after complete oxidation of the Li_6PS_5Cl−C electrode during the first charge the first discharge plateau is attributed to sulfur species reduction $(S \rightarrow S^{2-})$ and the second plateau is attributed to phosphorus species reduction $(P^{5+} \rightarrow P/P^{3-})$ as the only species remaining to be reduced is phosphorus. This hypothesis can be verified by directly discharging the Li−In | Li_6PS_5Cl | Li_6PS_5Cl−C cell from the OCV, as seen in Figure 2c. As the cell at the OCV is comprised of sulfur in its reduced state (S^{2-}) in Li_6PS_5Cl, directly discharging the cell will cause reduction of phosphorus species, as seen in the single discharge plateau at voltages below 1.3 V. On the basis of the previous computational predictions, Li_6PS_5Cl reduction will result in the formation of Li-containing products such as Li_3P, Li_2S, and $LiCl$.[13] To further test this hypothesis, we limit the reaction of phosphorus species by using a minimal amount of Li−In at the anode (Figure 2d). As the reduction of phosphorus species in Li_6PS_5Cl requires extra Li source to form the respective Li-containing products (e.g., Li_3P), these reactions cannot occur if all of the Li at the anode is fully consumed. As such, after being fully charged, only one discharge plateau attributed to sulfur redox was seen between 1.3 and 2.2 V. The galvanostatic data

as well as the cyclic voltammogram provides an indication of the SSE redox mechanism and the respective sulfur and phosphorus reaction potentials vs Li/Li$^+$. To support these findings, multiple characterization tools are utilized, and the results are discussed. Extended cycling of the Li−In | Li_6PS_5Cl | Li_6PS_5Cl−C cell can be found in Figure S1.

XPS of Li_6PS_5Cl at Various Potentials. To verify specific products of each sulfur or phosphorus species, XPS was conducted at each stage of charge (numbered 1−5 in Figure 3) for the S 2p, P 2p, and Cl 2p regions. Cycling profiles from Figure 2a are plotted vertically for ease of reference. At the pristine state, Li_6PS_5Cl is comprised of PS_4^{3-} thiophosphate units, which can be detected by the characteristic doublet peaks around 161.5 eV in the S 2p region and 131.5 eV in the P 2p region. This was described as terminal S bonds in some literature.[5,12] No signals from other components are found in the pristine electrolyte. Upon full charge of the Li−In | Li_6PS_5Cl | Li_6PS_5Cl−C cell to 4.2 V, Li_6PS_5Cl decomposes to form oxidized products of elemental S (Figure 3a-2) and P_2S_5 (Figure 3b-2). These findings agree with existing literature studies on the oxidation behavior of sulfide SSEs,[17] as well as computational studies showing Li_6PS_5Cl first forming LiCl and Li_3PS_4, followed by S and P_2S_5 upon further oxidation.[13]

Upon discharge of the cell until 1.3 V (Figure 3c-3), a decrease in peak intensities for S and P_2S_5 and a relative intensity increase of PS_4^{3-} thiophosphate characteristic energies are observed. This indicates a reformation of the PS_4^{3-} unit during cell discharge after oxidative decomposition of the pristine electrolyte. While its configuration and structural properties cannot be determined from XPS alone, it clearly suggests that Li_2S has not yet been formed after the first discharge plateau. Some residual signal is detected from unreacted P_2S_5 (Figure 3b-3). As it is believed to have poor

reaction kinetics, some P_2S_5 remains as partially irreversible products of Li_6PS_5Cl oxidation. Upon further discharge to 0 V, strong signals of Li_2S around 160 eV in Figure 3a-4 are observed, while weak signals of reduced phosphorus species and Li_3P are detected along with unreacted residual P_2S_5 in Figure 3b-4. It is worthy to note that due to the low stoichiometric ratio of P to S atoms in Li_6PS_5Cl signals from P 2p are weaker in relative intensity and difficult to detect. To verify that signals from P_2S_5 are attributed to oxidative species formed by charging to 4.2 V, another cell was prepared and directly discharged to 0 V from OCV (Figure 3c-5). As expected, no signals of P_2S_5 are detected, and only Li_2S, reduced P, and Li_3P are found (Figure 3b-5). Binding energies of the Cl 2p region can be found in Figure S2.

Two important observations can be made from the XPS study. (1) The decomposed product species at the oxidized state of 4.2 V and reduced state at 0 V represent the typical interfacial products of Li-ion ASSBs when Li_6PS_5Cl is used as the electrolyte. The half-cell setup used in this XPS study allows us to electrochemically form the thermodynamically driven interface products at typical voltages of oxide-based cathodes such as $LiCoO_2$ and anodes such as graphite, isolating any effects from the electrode material. (2) This study also demonstrates the reversibility of the electrolyte decomposition, where reformation of PS_4^{3-} units from elemental S and P_2S_5 acts as an intermediate redox product before formation of Li_2S when phosphorus is reduced at lower voltages.

XRD and Raman of Li_6PS_5Cl at Various Potentials. To substantiate these findings, X-ray diffraction (XRD) was conducted for the Li_6PS_5Cl-C cathode at similar cycling potentials (Figure 3d). At pristine states, diffraction peaks are observed at the characteristic Bragg angles of crystalline Li_6PS_5Cl, as seen in previous studies.[3,4,6] Unfortunately, there are little significant changes observed upon cell charging due to the poor symmetry and amorphous nature of oxidized S and P_2S_5 products, as reflected by an increased intensity of the amorphous bump between 20 and 30° at the 2θ. While any LiCl formed should be crystalline, its relative amounts are too low to be detected, and it is likely to be deposited as nanosized crystals as the SSE was pulverized during ball milling. Only signals from unreacted crystalline Li_6PS_5Cl can be detected. Likewise, the cell discharged to 1.3 V displays no significant change in diffraction patterns. However, the presence of oxidized elemental S can be detected clearly with Raman, as seen in Figure 3e. The charged Li_6PS_5Cl-C cathode at 4.2 V vs Li/Li^+ displays signals from oxidized S at 155, 220, and 475 cm^{-1}, electrolyte PS_4^{3-} at 430 cm^{-1}, as well as the D-band from CB at 1350 cm^{-1}. Upon further discharge to 0 V, the relative intensities of Li_6PS_5Cl diffraction peaks start to decrease. As phosphorus reduction in the electrolyte occurs, nanocrystalline Li_2S begins to form and is reflected as broad peaks seen at around 26, 45, and 52° at the 2θ (Figure 3d). A similar trend is observed for the cell that is directly discharged from the OCV. These findings are consistent with the XPS analysis discussed earlier, where elemental S is formed as a result of SSE oxidation during charging, Li_2S formation is not observed during discharge until low voltages, where phosphorus reduction occurs. Figure 4a illustrates the proposed reaction pathway of Li_6PS_5Cl reversible electrochemical redox based on the analysis discussed.

Solid-State Nuclear Magnetic Resonance (NMR) at the Mid-discharged State. To further characterize the nature of products at mid-discharge, ^6Li, ^7Li, and ^{31}P MAS NMR was conducted

by comparing pristine Li_6PS_5Cl to the mid-discharged state at 1.3 V. ^{31}P NMR spectra of the pristine and mid-discharged Li_6PS_5Cl material are shown in Figure 4b. The ^{31}P spectra of the pristine Li_6PS_5Cl are typical of that previously shown in literature,[46,47] with broad features centered at δ = 84.3 ppm and two low-frequency shoulders (δ = 82.7 and 81.0 ppm). The broadened features are caused by disorders on the anion sublattice from the substitutional mixing of Cl and S atoms on their respective crystallographic sites around the phosphorus PS_4^{3-} tetrahedron.[47] The ^{31}P spectrum of the mid-discharged Li_6PS_5Cl cathode bears the same broadened features as the pristine material with additional broadening at the tails. This difference is attributed to additional high-frequency broadening centered at around δ = 87 ppm, which falls in between the isotropic chemical shifts observed in crystalline γ-Li_3PS_4 (88.4 ppm) and β-Li_3PS_4 (86.53 ppm) phases.[48−50] This suggests the formation of isolated PS_4^{3-} tetrahedra with chemical environments more similar to those found in Li_3PS_4 than Li_6PS_5Cl. The broadening at very high (>90 ppm) and low (<82 ppm) frequencies is a result of an overall increase in the amorphous content of various PS_4^{3-} and $P_2S_7^{4-}$ units and covers a chemical shift distribution typical of Li-rich thiophosphate glasses.[51] The additional broadening observed after cycling suggests the increased presence of distorted PS_4^{3-} tetrahedra similar to that observed in Li_3PS_4 as well as a more heavily disordered thiophosphate network forming. Assigning definitive isotropic chemical shifts is challenging due to the extremely broadened features resulting from not only a distribution of bond lengths and angles of the PS_4^{3-} tetrahedra but also as a result of substitutional mixing of S and Cl within the second and third coordination spheres of Li_6PS_5Cl. However, deconvolution is performed to demonstrate an example of the rise of the distorted Li_3PS_4 and amorphous lithium thiophosphate components after cycling (Figure S4a). Evidence of residual Li_2S and LiCl after cycling is also found in $^{6,7}Li$ MAS NMR (Figure 4b). The ^7Li spectrum of the pristine material displays a single motional narrowed Lorentzian peak centered at 1.33 ppm. After cycling, the ^7Li spectrum displays a shift toward 1.2 ppm and a rise of a broad component between 0.5 and −2 ppm. These changes can be elucidated by comparison to the ^7Li chemical shifts for the reference compounds, Li_3PS_4 and LiCl (Figure S4). The ^7Li spectrum for Li_3PS_4 displays two peaks at 0.98 and 0.41 ppm, while LiCl displays one peak at −0.99 ppm. The increased intensity of the cycled Li_6PS_5Cl within these regions indicates the formation of a minor amount of these two compounds. However, a general lack of distinguishable features outside of the primary Li_6PS_5Cl peak suggests that Li^+ are exchanging within the chemical environments of these decomposed products. To obtain better resolution of these decomposed products, we turn to ^6Li MAS NMR (Figure 4c) as it offers an increased sensitivity to changes in the local structure compared to ^7Li. The relative difference of the primary Li_6PS_5Cl peak to the reference compounds, Li_3PS_4 and LiCl, is nearly the same as that seen in ^7Li. Comparing the pristine and cycled Li_6PS_5Cl material reveals the rise of a shallow broad component similar to that observed in the ^7Li spectrum. This broad component can be contributed to Li_3PS_4 and LiCl based on similarity of their ^6Li chemical shifts. The cycled Li_6PS_5Cl also shows a broadening toward higher chemical shift, which was notably absent from the ^7Li spectrum. This new feature is close to the chemical shift expected for Li_2S (2.35 ppm),[52] suggesting residual formation of $Li_{2−x}S$.
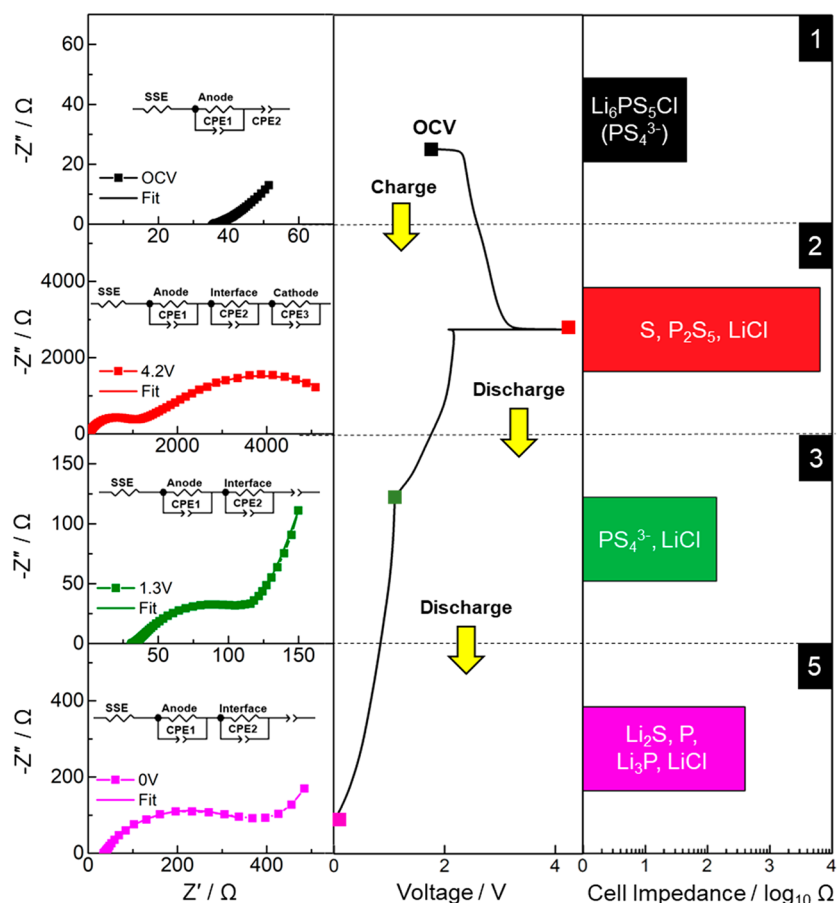
Figure 5. Nyquist plots at different cycling potentials showing the impedance changes of the Li−In | LPSCl | LPSCl-C cell (left). Normalized capacity vs voltage profiles are displayed for reference (middle). The bar graph shows relative differences in cell impedance at different oxidation or reduction states of $Li_6PS_5Cl−C$ (right); direct discharge (marked as 5) is used at the full reduced state for fair comparison.

*EIS of the Li_6PS_5Cl Half-Cell at Various Potentials.* Next, we investigate the impact of Li_6PS_5Cl decomposition products on cell impedance in typical Li-ion ASSBs. To do so, we conduct electrochemical impedance spectroscopy (EIS) measurements across the Li−In | Li_6PS_5Cl | Li_6PS_5Cl−C cell at different cycling potentials (Figure 5). Considering that charge transfer resistances at the Li−In anode and of the bulk electrolyte do not change significantly, any changes in total cell impedance can be attributed to impedance growth or ionic conductivity changes in the Li_6PS_5Cl−C electrode as redox proceeds.

A Nyquist plot of the pristine cell at the OCV shows a total cell resistance of approximately 45 Ω, which translates into the expected Li_6PS_5Cl conductivity on the order of $\sim10^{-3}$ S cm^{-1}. However, when the cell is charged, the total cell resistance increases by 2 orders of magnitude, as reflected in Figure 5 (left). This results from formation of highly insulating products of S and P_2S_5, dramatically increasing the charge transfer resistance in the cathode. However, when the cell is discharged to 1.3 V, the total cell impedance falls to 139 Ω, as seen in the bar chart of Figure 5 (right), regaining almost all of the conductive properties of the electrolyte in the cathode. This is due to the reformation of conductive Li_3PS_4 found in the previous section. It is likely that the impedance measured at 1.3 V is higher than that of the pristine state due to incomplete reaction of the oxidized products found in Figure 3b as well as contributions from LiCl formed during redox. Upon full discharge to 0 V, the total cell impedance increases to 400 Ω (Figure 5), which is an increase of less than 1 order of

magnitude compared to the pristine state. The large changes in impedances measured across the cell during cycling provides us an indication of the effects of SSE decomposition on ASSB cell performance.

Li_6PS_5Cl Reductive Decomposition. From these results, it can be inferred that impedance growth in ASSB full cells during cycling is largely attributed to oxidation decomposition of SSE at high voltages. By comparison, reduction decomposition of SSEs at anodes such as graphite contributes less to cell resistance. This likely results from the formation of Li_3P, which was previously reported to have some Li$^+$ conductive properties.[53,54] Additionally, on the basis of literature work studying Li−S chemistries, Li_2S at discharged states was found to have comparatively lower charge transfer resistances compared to elemental S at charged states when measured with similar impedance methods.[55] To further substantiate this, impedance growth of an anode composite comprising 60 wt % carbon graphite was measured before and after lithiation (Figure S5). As expected, impedance growth at the anode was still significantly less compared to that of the cathode composite comprising only 1 wt % CB after charging. EIS measurements were also done on pure interfacial components prepared in their stoichiometric formation ratios. The results showed some ionic conductive properties of reduced species ($\sim10^{-6}$ S cm^{-1}), while the oxidized species were found to be entirely insulative (Figure S6).

Li_6PS_5Cl Oxidative Decomposition. While SSE decomposition brings about negative effects on electrode charge transfer
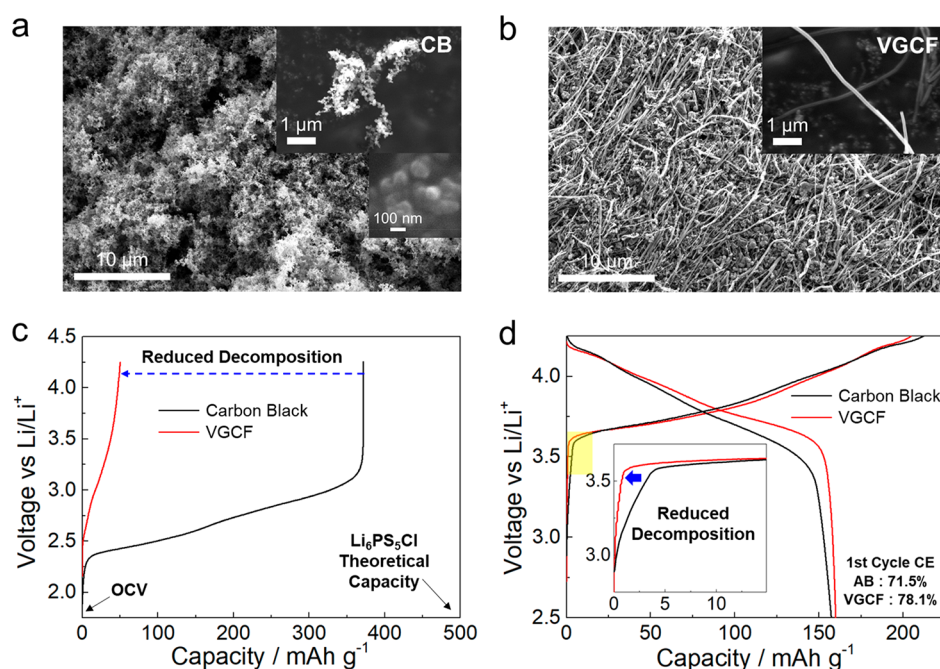
Figure 6. SEM images of (a) CB and (b) VGCF showing differences in morphology and size. (c) Charge voltage profiles of Li−In ∣ Li$_6$PS$_5$Cl ∣ Li$_6$PS$_5$Cl−C cells using 30 wt % CB (surface area: ∼80 m^2/g) vs VGCF (surface area: ∼24 m^2/g)). (d) Charge and discharge voltage profiles of Li−In ∣ Li$_6$PS$_5$Cl ∣ NCM811 cells using 1 wt % of CB vs VGCF.

resistance and overall cell impedance, its impact is more pronounced at the cathode where oxidative decomposition occurs. As such, strategies to mitigate SSE oxidative decomposition in ASSBs are vital. Although it is difficult to change the decomposition thermodynamics of sulfide-based SSEs, it is possible to control its kinetics by tuning the morphology or specific surface area of carbon used. With reduced surface area, the SSE would have less exposure to electronically conductive surfaces. Without a sufficient electronic pathway for redox to occur, the kinetics of SSE decomposition can be significantly reduced.

Due to its nanosized particles (Figure 6a), CB has a higher specific surface area (80 m^2 g^{-1}) that promotes decomposition kinetics of SSEs compared to other types of carbon such as vapor-grown carbon fiber (VGCF) with lower surface area (24 m^2 g^{-1}) (Figure 6b). Such differences were also detected with Raman, where VGCF exhibits significantly lowered D/G band ratios compared to CB (Figure S3). Figure 6c illustrates the effect of using 30 wt % of both types of carbon in the Li−In ∣ Li$_6$PS$_5$Cl ∣ Li$_6$PS$_5$Cl−C cell charged at 0.25 mA cm^{-2}. The cell using CB showed much higher decomposition capacity and faster decomposition kinetics compared to the cell using VGCF. The sharp vertical voltage line at the end of the plateau of the SSE−CB composite also indicates a complete reaction of SSE in the composite, while the VGCF composite shows a higher polarization, indicating decreased decomposition kinetics. The effect of using lower surface area carbon can also be seen in Figure 6d, which compares the first cycle cell voltage curves of a Li−In ∣ Li$_6$PS$_5$Cl ∣ NCM811 half-cell using 1 wt % of each carbon type in the oxide cathode. The cell using VGCF carbon additive shows a reduced electrolyte decomposition profile offset (inset), as well as a higher first cycle coulombic efficiency compared to CB. Additionally, the discharge curve from the cell using VGCF also displays lower cell polarization. This results from lower cell impedance due to reduced SSE decomposition compared to the cell using

CB. Extended cycling capacity retentions can be found in Figure S7.

As such, scientific efforts to improve the performance of ASSBs such as widening of the SSE's electrochemical stability window and/or reducing cell polarization growth over extended cycling can be directed toward reducing electrolyte oxidative decomposition. However, this is challenging to overcome as the oxidative decomposition during the first charge is an unavoidable thermodynamic property of the electrolyte. Existing methods to apply surface coatings on the cathode particles can only reduce the interfacial reactions between the electrolyte and electrode but cannot prevent the formation of highly resistive oxidized SSE products. Current efforts to tackle this by controlling the decomposition kinetics should go beyond carbon optimization or using materials with lower specific surface area at the cathode as carbon still plays an important role in capacity utilization of layered oxide cathodes. Other strategies are needed to either improve the intrinsic property of the SSE or further reduce its decomposition kinetics. New methods may include surface or bulk modification of SSE particles to improve their stability at high voltage or developing better conductive networks to maintain an electronic pathway between cathode particles with minimal exposure to the SSE.

In summary, this study elucidates the redox behavior and the mechanisms of Li$_6$PS$_5$Cl solid electrolyte decomposition. We found that Li$_6$PS$_5$Cl decomposition is irreversible in Li-ion batteries due to the high voltage ranges used. When lower voltage cycling is done, large reversible capacities of 965 mAh g^{-1} from the electrolyte alone are observed. To investigate this reversible decomposition, XPS, XRD, Raman, and NMR characterizations were conducted at various voltages of a Li−In ∣ Li$_6$PS$_5$Cl ∣ Li$_6$PS$_5$Cl−C cell, where its oxidation and reduction products were identified experimentally. It was found that oxidized products of elemental S and P$_2$S$_5$ undergo an intermediate transition product of Li$_3$PS$_4$ before being

reduced to Li$_2$S and Li$_3$P. Subsequently, the impedance contributions of reductive and oxidative decomposition products were measured using EIS measurements. It was found that the cell impedance and polarization growth in typical Li-ion ASSBs are a result of SSE decomposition at the cathode, where reductive SSE decomposition has less effect on overall cell impedance. Alternative types of low specific surface area carbon are proposed to reduce SSE decomposition, and its effect was demonstrated in a Li–In | Li$_6$PS$_5$Cl | NCM811 cell. The principles of SSE redox and its mechanism found in this study can be further extended toward new electrolyte material selection or modification that mitigates SSE oxidation decomposition and thus improves cycle performance of ASSBs.

■ ASSOCIATED CONTENT

Ⓢ Supporting Information

The Supporting Information is available free of charge on the ACS Publications website at DOI: 10.1021/acsenergy-lett.9b01693.

> Experimental Details, literature Li–S ASSBs summary table, Li$_6$PS$_5$Cl–C half-cell cycling with different voltage windows, XPS binding energies of Cl 2p regions, Raman spectra of CB vs vapor-grown carbon fiber, NMR chemical shifts of ^{31}P and ^{6,7}Li reference materials, anode vs cathode impedance growth comparison, reduced vs oxidized species impedance comparison, and extended half-cell cycle capacity retention (PDF)

■ AUTHOR INFORMATION

Corresponding Authors
*E-mail: a7banerjee@eng.ucsd.edu.
*E-mail: shirleymeng@ucsd.edu.
ORCID Ⓞ
Zheng Chen: 0000-0002-9186-4298
Xuefeng Wang: 0000-0001-9666-8942
Ying Shirley Meng: 0000-0001-8936-8845
Notes
The authors declare no competing financial interest.

■ ACKNOWLEDGMENTS

■ REFERENCES

(1) Jung, Y. S.; Oh, D. Y.; Nam, Y. J.; Park, K. H. Issues and Challenges for Bulk-Type All-Solid-State Rechargeable Lithium Batteries using Sulfide Solid Electrolytes. *Isr. J. Chem.* **2015**, *55* (5), 472–485.

(2) Kerman, K.; Luntz, A.; Viswanathan, V.; Chiang, Y.-M.; Chen, Z. Review—Practical Challenges Hindering the Development of Solid State Li Ion Batteries. *J. Electrochem. Soc.* **2017**, *164* (7), A1731–A1744.

(3) Yu, C.; van Eijck, L.; Ganapathy, S.; Wagemaker, M. Synthesis, structure and electrochemical performance of the argyrodite Li$_6$PS$_5$Cl solid electrolyte for Li-ion solid state batteries. *Electrochim. Acta* **2016**, *215*, 93–99.

(4) Yu, C.; Ganapathy, S.; Hageman, J.; van Eijck, L.; van Eck, E. R. H.; Zhang, L.; Schwietert, T.; Basak, S.; Kelder, E. M.; Wagemaker, M. Facile Synthesis toward the Optimal Structure-Conductivity Characteristics of the Argyrodite Li$_6$PS$_5$Cl Solid-State Electrolyte. *ACS Appl. Mater. Interfaces* **2018**, *10* (39), 33296–33306.

(5) Auvergniot, J.; Cassel, A.; Ledeuil, J. B.; Viallet, V.; Seznec, V.; Dedryvère, R. Interface Stability of Argyrodite Li$_6$PS$_5$Cl toward LiCoO$_2$, LiNi$_{1/3}$Co$_{1/3}$Mn$_{1/3}$O$_2$, and LiMn$_2$O$_4$ in Bulk All-Solid-State Batteries. *Chem. Mater.* **2017**, *29*, 3883–3890.

(6) Wang, S.; Zhang, Y.; Zhang, X.; Liu, T.; Lin, Y. H.; Shen, Y.; Li, L.; Nan, C. W. High-Conductivity Argyrodite Li$_6$PS$_5$Cl Solid Electrolytes Prepared via Optimized Sintering Processes for All-Solid-State Lithium-Sulfur Batteries. *ACS Appl. Mater. Interfaces* **2018**, *10*, 42279–42285.

(7) Wenzel, S.; Weber, D. A.; Leichtweiss, T.; Busche, M. R.; Sann, J.; Janek, J. Interphase formation and degradation of charge transfer kinetics between a lithium metal anode and highly crystalline Li$_7$P$_3$S$_{11}$ solid electrolyte. *Solid State Ionics* **2016**, *286*, 24–33.

(8) Wenzel, S.; Randau, S.; Leichtweiß, T.; Weber, D. A.; Sann, J.; Zeier, W. G.; Janek, J. Direct Observation of the Interfacial Instability of the Fast Ionic Conductor Li$_{10}$GeP$_2$S$_{12}$ at the Lithium Metal Anode. *Chem. Mater.* **2016**, *28*, 2400–2407.

(9) Kato, Y.; Hori, S.; Saito, T.; Suzuki, K.; Hirayama, M.; Mitsui, A.; Yonemura, M.; Iba, H.; Kanno, R. High-power all-solid-state batteries using sulfide superionic conductors. *Nat. Energy* **2016**, *1*, 16030.

(10) Sakuda, A.; Hayashi, A.; Tatsumisago, M. Interfacial Observation between LiCoO$_2$ Electrode and Li$_2$S–P$_2$S$_5$ Solid Electrolytes of All-Solid-State Lithium Secondary Batteries Using Transmission Electron Microscopy. *Chem. Mater.* **2010**, *22* (3), 949–956.

(11) Hakari, T.; Deguchi, M.; Mitsuhara, K.; Ohta, T.; Saito, K.; Orikasa, Y.; Uchimoto, Y.; Kowada, Y.; Hayashi, A.; Tatsumisago, M. Structural and Electronic-State Changes of a Sulfide Solid Electrolyte during the Li Deinsertion–Insertion Processes. *Chem. Mater.* **2017**, *29* (11), 4768–4774.

(12) Swamy, T.; Chen, X.; Chiang, Y.-M. Electrochemical Redox Behavior of Li Ion Conducting Sulfide Solid Electrolytes. *Chem. Mater.* **2019**, *31* (3), 707–713.

(13) Zhu, Y.; He, X.; Mo, Y. Origin of Outstanding Stability in the Lithium Solid Electrolyte Materials: Insights from Thermodynamic Analyses Based on First-Principles Calculations. *ACS Appl. Mater. Interfaces* **2015**, *7* (42), 23685–23693.

(14) Richards, W. D.; Miara, L. J.; Wang, Y.; Kim, J. C.; Ceder, G. Interface Stability in Solid-State Batteries. *Chem. Mater.* **2016**, *28* (1), 266–273.

(15) Zhang, W.; Leichtweiss, T.; Culver, S. P.; Koerver, R.; Das, D.; Weber, D. A.; Zeier, W. G.; Janek, J. The Detrimental Effects of Carbon Additives in Li$_{10}$GeP$_2$S$_{12}$-Based Solid-State Batteries. *ACS Appl. Mater. Interfaces* **2017**, *9* (41), 35888–35896.

(16) Koerver, R.; Aygün, I.; Leichtweiß, T.; Dietrich, C.; Zhang, W.; Binder, J. O.; Hartmann, P.; Zeier, W. G.; Janek, J. Capacity Fade in Solid-State Batteries: Interphase Formation and Chemomechanical Processes in Nickel-Rich Layered Oxide Cathodes and Lithium Thiophosphate Solid Electrolytes. *Chem. Mater.* **2017**, *29*, 5574–5582.

(17) Auvergniot, J.; Cassel, A.; Foix, D.; Viallet, V.; Seznec, V.; Dedryvère, R. Redox activity of argyrodite Li$_6$PS$_5$Cl electrolyte in all-solid-state Li-ion battery: An XPS study. *Solid State Ionics* **2017**, *300*, 78–85.

(18) Suzuki, K.; Mashimo, N.; Ikeda, Y.; Yokoi, T.; Hirayama, M.; Kanno, R. High Cycle Capability of All-Solid-State Lithium–Sulfur Batteries Using Composite Electrodes by Liquid-Phase and

Mechanical Mixing. *ACS Appl. Mater. Interfaces* **2018**, *1* (6), 2373–2377.

(19) Han, F.; Gao, T.; Zhu, Y.; Gaskell, K. J.; Wang, C. A Battery Made from a Single Material. *Adv. Mater.* **2015**, *27* (23), 3473–83.

(20) Yamada, T.; Ito, S.; Omoda, R.; Watanabe, T.; Aihara, Y.; Agostini, M.; Ulissi, U.; Hassoun, J.; Scrosati, B. All Solid-State Lithium–Sulfur Battery Using a Glass-Type P_2S_5–Li_2S Electrolyte: Benefits on Anode Kinetics. *J. Electrochem. Soc.* **2015**, *162* (4), A646–A651.

(21) Kobayashi, T.; Imade, Y.; Shishihara, D.; Homma, K.; Nagao, M.; Watanabe, R.; Yokoi, T.; Yamada, A.; Kanno, R.; Tatsumi, T. All solid-state battery with sulfur electrode and thio-LISICON electrolyte. *J. Power Sources* **2008**, *182* (2), 621–625.

(22) Kinoshita, S.; Okuda, K.; Machida, N.; Naito, M.; Sigematsu, T. All-solid-state lithium battery with sulfur/carbon composites as positive electrode materials. *Solid State Ionics* **2014**, *256*, 97–102.

(23) Machida, N. Electrochemical properties of sulfur as cathode materials in a solid-state lithium battery with inorganic solid electrolytes. *Solid State Ionics* **2004**, *175* (1–4), 247–250.

(24) Nagao, M.; Hayashi, A.; Tatsumisago, M. High-capacity Li_2S–nanocarbon composite electrode for all-solid-state rechargeable lithium batteries. *J. Mater. Chem.* **2012**, *22* (19), 10015.

(25) Lin, Z.; Liu, Z.; Fu, W.; Dudney, N. J.; Liang, C. Lithium polysulfidophosphates: a family of lithium-conducting sulfur-rich compounds for lithium-sulfur batteries. *Angew. Chem., Int. Ed.* **2013**, *52* (29), 7460–7463.

(26) Hayashi, A.; Ohtsubo, R.; Ohtomo, T.; Mizuno, F.; Tatsumisago, M. All-solid-state rechargeable lithium batteries with Li2S as a positive electrode material. *J. Power Sources* **2008**, *183* (1), 422–426.

(27) Hayashi, A.; Ohtomo, T.; Mizuno, F.; Tadanaga, K.; Tatsumisago, M. Rechargeable lithium batteries, using sulfur-based cathode materials and Li_2S–P_2S_5 glass-ceramic electrolytes. *Electrochim. Acta* **2004**, *50* (2–3), 893–897.

(28) Nagao, M.; Hayashi, A.; Tatsumisago, M. Sulfur–carbon composite electrode for all-solid-state Li/S battery with Li_2S–P_2S_5 solid electrolyte. *Electrochim. Acta* **2011**, *56* (17), 6055–6059.

(29) Nagao, M.; Hayashi, A.; Tatsumisago, M. Fabrication of favorable interface between sulfide solid electrolyte and Li metal electrode for bulk-type solid-state Li/S battery. *Electrochem. Commun.* **2012**, *22*, 177–180.

(30) Nagata, H.; Chikusa, Y. Activation of sulfur active material in an all-solid-state lithium–sulfur battery. *J. Power Sources* **2014**, *263*, 141–144.

(31) Lin, Z.; Liu, Z.; Dudney, N. J.; Liang, C. Lithium Superionic Sulfide Cathode for All-Solid Lithium–Sulfur Batteries. *ACS Nano* **2013**, *7* (3), 2829–2833.

(32) Agostini, M.; Aihara, Y.; Yamada, T.; Scrosati, B.; Hassoun, J. A lithium–sulfur battery using a solid, glass-type P_2S_5–Li_2S electrolyte. *Solid State Ionics* **2013**, *244*, 48–51.

(33) Nagao, M.; Hayashi, A.; Tatsumisago, M.; Ichinose, T.; Ozaki, T.; Togawa, Y.; Mori, S. Li_2S nanocomposites underlying high-capacity and cycling stability in all-solid-state lithium–sulfur batteries. *J. Power Sources* **2015**, *274*, 471–476.

(34) Nagao, M.; Imade, Y.; Narisawa, H.; Kobayashi, T.; Watanabe, R.; Yokoi, T.; Tatsumi, T.; Kanno, R. All-solid-state Li–sulfur batteries with mesoporous electrode and thio-LISICON solid electrolyte. *J. Power Sources* **2013**, *222*, 237–242.

(35) Choi, H. U.; Jin, J. S.; Park, J.-Y.; Lim, H.-T. Performance improvement of all-solid-state Li-S batteries with optimizing morphology and structure of sulfur composite electrode. *J. Alloys Compd.* **2017**, *723*, 787–794.

(36) Hayashi, A.; Ohtomo, T.; Mizuno, F.; Tadanaga, K.; Tatsumisago, M. All-solid-state Li/S batteries with highly conductive glass–ceramic electrolytes. *Electrochem. Commun.* **2003**, *5* (8), 701–705.

(37) Hayashi, A.; Ohtsubo, R.; Tatsumisago, M. Electrochemical performance of all-solid-state lithium batteries with mechanochemi-cally activated Li_2S–Cu composite electrodes. *Solid State Ionics* **2008**, *179* (27–32), 1702–1705.

(38) Nagata, H.; Chikusa, Y. A lithium sulfur battery with high power density. *J. Power Sources* **2014**, *264*, 206–210.

(39) Trevey, J. E.; Gilsdorf, J. R.; Stoldt, C. R.; Lee, S. H.; Liu, P. Electrochemical Investigation of All-Solid-State Lithium Batteries with a High Capacity Sulfur-Based Electrode. *J. Electrochem. Soc.* **2012**, *159* (7), A1019–A1022.

(40) Zhang, Y.; Liu, T.; Zhang, Q.; Zhang, X.; Wang, S.; Wang, X.; Li, L.; Fan, L.-Z.; Nan, C.-W.; Shen, Y. High-performance all-solid-state lithium–sulfur batteries with sulfur/carbon nano-hybrids in a composite cathode. *J. Mater. Chem. A* **2018**, *6* (46), 23345–23356.

(41) Yan, H.; Wang, H.; Wang, D.; Li, X.; Gong, Z.; Yang, Y. In Situ Generated Li_2S-C Nanocomposite for High-Capacity and Long-Life All-Solid-State Lithium Sulfur Batteries with Ultrahigh Areal Mass Loading. *Nano Lett.* **2019**, *19*, 3280–3287.

(42) Xu, R.; Yue, J.; Liu, S.; Tu, J.; Han, F.; Liu, P.; Wang, C. Cathode-Supported All-Solid-State Lithium–Sulfur Batteries with High Cell-Level Energy Density. *ACS Energy Lett.* **2019**, *4*, 1073–1079.

(43) Han, F.; Yue, J.; Fan, X.; Gao, T.; Luo, C.; Ma, Z.; Suo, L.; Wang, C. High-Performance All-Solid-State Lithium-Sulfur Battery Enabled by a Mixed-Conductive Li_2S Nanocomposite. *Nano Lett.* **2016**, *16* (7), 4521–4527.

(44) Takeuchi, T.; Kageyama, H.; Nakanishi, K.; Tabuchi, M.; Sakaebe, H.; Ohta, T.; Senoh, H.; Sakai, T.; Tatsumi, K. All-Solid-State Lithium Secondary Battery with Li_2S–C Composite Positive Electrode Prepared by Spark-Plasma-Sintering Process. *J. Electrochem. Soc.* **2010**, *157* (11), A1196.

(45) Hakari, T.; Nagao, M.; Hayashi, A.; Tatsumisago, M. All-solid-state lithium batteries with Li_3PS_4 glass as active material. *J. Power Sources* **2015**, *293*, 721–725.

(46) Hanghofer, I.; Gadermaier, B.; Wilkening, H. M. R. Fast Rotational Dynamics in Argyrodite-Type Li_6PS_5X (X: Cl, Br, I) as Seen by ^{31}P Nuclear Magnetic Relaxation—On Cation–Anion Coupled Transport in Thiophosphates. *Chem. Mater.* **2019**, *31* (12), 4591–4597.

(47) Deiseroth, H. J.; Kong, S. T.; Eckert, H.; Vannahme, J.; Reiner, C.; Zaiss, T.; Schlosser, M. Li_6PS_5X: a class of crystalline Li-rich solids with an unusually high Li+ mobility. *Angew. Chem., Int. Ed.* **2008**, *47* (4), 755–758.

(48) Gobet, M.; Greenbaum, S.; Sahu, G.; Liang, C. Structural Evolution and Li Dynamics in Nanophase Li_3PS_4 by Solid-State and Pulsed-Field Gradient NMR. *Chem. Mater.* **2014**, *26* (11), 3558–3564.

(49) Eckert, H.; Zhang, Z.; Kennedy, J. H. Structural Trans-formation of Non-Oxide Chalcogenide Glasses. The Short-Range Order of Li_2S-P_2S_5 Glasses Studied by Quantitative ^{31}P and $^{6,7}Li$ High-Resolution Solid-State NMR. *Chem. Mater.* **1990**, *2*, 273–279.

(50) Stöffler, H.; Zinkevich, T.; Yavuz, M.; Hansen, A.-L.; Knapp, M.; Bednarčík, J.; Randau, S.; Richter, F. H.; Janek, J.; Ehrenberg, H.; Indris, S. Amorphous versus Crystalline Li_3PS_4: Local Structural Changes during Synthesis and Li Ion Mobility. *J. Phys. Chem. C* **2019**, *123* (16), 10280–10290.

(51) Seino, Y.; Nakagawa, M.; Senga, M.; Higuchi, H.; Takada, K.; Sasaki, T. Analysis of the structure and degree of crystallisation of $70Li_2S$–$30P_2S_5$ glass ceramic. *J. Mater. Chem. A* **2015**, *3* (6), 2756–2761.

(52) Huff, L. A.; Rapp, J. L.; Baughman, J. A.; Rinaldi, P. L.; Gewirth, A. A. Identification of lithium–sulfur battery discharge products through ^6Li and ^{33}S solid-state MAS and ^7Li solution NMR spectroscopy. *Surf. Sci.* **2015**, *631*, 295–300.

(53) Lin, L.; Liang, F.; Zhang, K.; Mao, H.; Yang, J.; Qian, Y. Lithium phosphide/lithium chloride coating on lithium for advanced lithium metal anode. *J. Mater. Chem. A* **2018**, *6* (32), 15859–15867.

(54) Nazri, G. Preparation, Structure and Ionic Conductivity of Lithium Phosphide. *Solid State Ionics* **1989**, *34*, 97–102.

(55) Deng, Z.; Zhang, Z.; Lai, Y.; Liu, J.; Li, J.; Liu, Y. Electrochemical Impedance Spectroscopy Study of a Lithium/Sulfur

Battery: Modeling and Analysis of Capacity Fading. *J. Electrochem. Soc.* **2013**, *160* (4), A553−A558.